PLOS ONE

RESEARCH ARTICLE

Cardiac digital twins at scale from MRI: Open tools and representative models from ~ 55000 UK Biobank participants

Devran Ugurlu[1,2,3☯*], **Shuang Qian**[1,2☯], **Elliot Fairweather**[1☯], **Charlene Mauger**[1], **Bram Ruijsink**[1,4], **Laura Dal Toso**[5], **Yu Deng**[1], **Marina Strocchi**[1,2,3], **Reza Razavi**[1], **Alistair Young**[1‡], **Pablo Lamata**[1‡], **Steven Niederer**[1,2,3‡], **Martin Bishop**[1‡]

1 School of Biomedical Engineering and Imaging Sciences, King's College London, London, United Kingdom, **2** The Cardiac Electro-Mechanics Research Group, Imperial College London, London, United Kingdom, **3** The Alan Turing Institute, London, United Kingdom, **4** Department of Cardiology, University Medical Center Utrecht, Utrecht, The Netherlands, **5** Institute for Biomedical Engineering, University and ETH Zurich, Zurich, Switzerland

☯ These authors contributed equally to this work.
‡ These authors also contributed equally to this work.
* devran.ugurlu@kcl.ac.uk

OPEN ACCESS

Citation: Ugurlu D, Qian S, Fairweather E, Mauger C, Ruijsink B, Toso LD, et al. (2025) Cardiac digital twins at scale from MRI: Open tools and representative models from 55000 UK Biobank participants. PLoS One 20(7): e0327158. https://doi.org/10.1371/journal.pone.0327158

Editor: Roberto Magalhães Saraiva, Oswaldo Cruz Foundation, BRAZIL

Received: January 3, 2025

Accepted: June 10, 2025

Published: July 15, 2025

Data availability statement: Some of the data, namely individual patient data, is only accessible through UK Biobank. This includes individual cine MRs and demographics information such as age and BMI. The manual segmentations, which are individual derived data generated by the authors, will be returned to the UK Biobank and will be accessible through their data return mechanism (project ID: 88878). To gain access to UK Biobank data, researchers must go through their established application procedure which can be found at

Abstract

A cardiac digital twin is a virtual replica of a patient's heart for screening, diagnosis, prognosis, risk assessment, and treatment planning of cardiovascular diseases. This requires an anatomically accurate patient-specific 3D structural representation of the heart, suitable for electro-mechanical simulations or study of disease mechanisms. However, generation of cardiac digital twins at scale is demanding and there are no public repositories of models across demographic groups. We describe an automatic open-source pipeline for creating patient-specific left and right ventricular meshes from cardiovascular magnetic resonance images, its application to a large cohort of ~ 55k participants from UK Biobank, and the construction of the most comprehensive cohort of adult heart models to date, comprising 1423 representative meshes across sex (male, female), body mass index (range: 16–42 kg/m^2) and age (range: 49–80 years). Our code is available at https://github.com/cdttk/biv-volumetric-meshing/tree/plos2025, and pre-trained networks, representative volumetric meshes with fibers and UVCs are available at https://doi.org/10.5281/zenodo.15649643.

Introduction

Approximately one-third of deaths globally are estimated to be caused by cardiovascular diseases [1]. A Cardiac Digital Twin (CDT) aims to improve cardiac healthcare by creating a virtual replica of a patient's heart through an interdisciplinary approach in personalized medicine. The CDT can, in principle, be used to improve risk assessment, screening, diagnosis, and treatment by providing more accurate personalised in silico monitoring and predictions compared to traditional methods [2–4]. A CDT is continuously updated with new relevant data - these data can be periodically acquired in hospital visits, including imaging

http://www.ukbiobank.ac.uk/register-apply/. All the generated data that we are legally allowed to share are publicly available at https://doi.org/10.5281/zenodo.15649643. This includes the weights of trained segmentation networks, representative volumetric meshes with fibers, and their corresponding UVCs.

Funding: This work was supported primarily by the Wellcome EPSRC Centre for Medical Engineering (WT203148/Z/16/Z). Besides, SN is supported by Engineering and Physical Sciences Research Council (EP/X012603/1, EP/P01268X/1, EP/X03870X/1), British Heart Foundation (RG/20/4/34803), Foundation for the National Institutes of Health (R01-HL152256) and European Research Council (PREDICT-HF 453 (864055)). MB is supported by British Heart Foundation (PG/22/10871, PG/22/11159, PG/18/74/34077). AY is supported by Foundation for the National Institutes of Health (R01-HL121754) and Engineering and Physical Sciences Research Council (EP/Z533762/1). MS is supported by British Heart Foundation(RE/18/4/34215) and NIHR Imperial Biomedical Research Centre. PL is supported by King's British Heart Foundation (BHF) Centre of Research Excellence (RE/24/130035) and Wellcome Trust (209450/Z/17/Z). The funders did not play any role in the study design, data collection and analysis, decision to publish, or preparation of the manuscript. URLs of funder websites are as follows: Foundation for the National Institutes of Health (https://www.nih.gov/), European Research Council (https://erc.europa.eu/homepage), British Heart Foundation (https://www.bhf.org.uk/), Engineering and Physical Sciences Research Council (https://www.ukri.org/councils/epsrc/), Wellcome EPSRC Centre for Medical Engineering (https://www.kcl.ac.uk/research/centre-for-medical-engineering-1), NIHR Imperial Biomedical Research Centre (https://imperialbrc.nihr.ac.uk/), King's British Heart Foundation (BHF) Centre of Research Excellence (https://www.kcl.ac.uk/scmms/bhf-centre), Wellcome Trust (https://wellcome.org/).

Competing interests: The authors have declared that no competing interests exist.

studies, or can be acquired real-time, e.g. with wearable devices. A CDT-based monitoring and prediction system may involve a variety of components such as mechanistic simulation, statistical prediction models, many types of data sources, and secure data storage and transfer protocols [2–4].

In this context, CDTs based on recapitulating the anatomy and function of the ventricles of the heart are being used to predict sudden cardiac death risks [5], guide the placements of implanted devices [6], plan ablation procedures [7], better predict adverse cardiovascular events [8], and provide mechanistic insights in public health by inferring patient-specific myocardial tissue properties [9], among others. A key requirement in all these applications is the ability to personalise a bi-ventricular cardiac computational mesh to each patient.

Cardiovascular Magnetic Resonance (CMR) images are routinely acquired in clinical practice for calculating diagnostic metrics such as left and right ventricular (LV and RV) volumes and ejection fraction (EF) [10,11]. CMR acquisitions typically consist of multiple 2D cine steady state free precision scans, leading to a set of slices in heart's short axis (SAX), usually 8–12 slices with a thickness around 8–10 mm, and one to three circumferentially sampled long axis (LAX) slices [12,13]. Due to the sparse and cross-sectional nature of the slices, and the fact that the slices might be misaligned due to patient movement and differences in breath-hold position during acquisition, it is not straightforward to reconstruct the 3D structure from these 2D images [12,13]. Hence, this problem has been an active research area and a variety of methods have been proposed.

One approach is to tackle the problem at the imaging protocol and reconstruction stage and attempt to create an isotropic 3D cine image through faster undersampled scans and smart image reconstruction using deep-learning models instead of classical reconstruction algorithms [14–16]. While this approach shows promise for future applications, 2D cine is still the clinical standard and most existing cine MR datasets are acquired using the 2D clinical standard.

The methods proposed for 3D heart mesh reconstruction from typical clinical cine MR acquisitions have included three common approaches: deforming an initial/template mesh to fit the CMR data, fitting to a statistical shape model (SSM), and deep-learning based reconstruction. [17] warped a template mesh to fit the anatomy through registration of binary images created from the template mesh and segmentation of the medical image. [18] and [13] deformed an initial mesh to a point cloud obtained from contours of extracted relevant structures such as the LV endocardium and epicardium, and RV endocardium after segmentation. In [19], a template biventricular heart mesh is deformed under diffeomorphic constraints to a point cloud consisting of contours and landmarks extracted from CMR images. [20] proposed a deep-learning approach where a point cloud completion network was trained to convert the sparse point cloud extracted from CMR images to a dense point cloud. In [21], a multi-step whole-heart mesh reconstruction method was proposed where the contours extracted from CMR images were first used to reconstruct a biventricular mesh, which was then fitted to a whole-heart SSM created from high-resolution CT by [22]. As a final step, the whole-heart mesh was deformed using the method proposed in [18]. [23] proposed a heart shape reconstruction method based on learning the principal component analysis parameters of a point distribution model. The training set was created by registering the cardiac atlas mesh from [24] to manual contours extracted from CMR. This method simultaneously used the SAX view, 3 LAX views and patient metadata in the learning process. [25] directly created a volumetric mesh from CMR images using a graph convolution network. The training set was created in the same way as [23]. [26,27] proposed two similar whole-heart mesh reconstruction methods based on learning mesh deformations using graph convolution networks coupled with a segmentation module. The methods were demonstrated to work with 3D CT, 3D MR

and cine MR images. Although these methods are capable in principle of deriving digital twin representative models at scale, none have done so. The existing methods have one or more of the following limitations: either they did not explicitly model the locations of the aorta, mitral and tricuspid valves from available long axis images, or they were not demonstrated to work at scale (>50k cases), or source code is not publicly available.

Reconstructing the 3D heart shape from CMR images requires considerable effort and expertise. Additionally, creating a full CDT system may be a complex interdisciplinary endeavour, and researchers that work on one particular part of the system may not be familiar with another part. Therefore, it is imperative that both open source tools and publicly available outputs are provided that can be readily used by researchers who work on other parts of the CDT system. This paper aims to facilitate cardiac digital twinning with the following contributions:

1. A fully open source automatic pipeline from raw cine MR images to biventricular meshes. The method is validated on UKBB data and can both act as a baseline for other researchers who are working on the same problem, or can be used to easily create patient-specific meshes from cine MR images.
2. 1423 publicly available representative meshes created from different sex, BMI, and age groupings. This diverse set of meshes can be readily used by other CDT researchers who use biventricular meshes as input to their work, such as researchers working on mechanistic simulation or statistical prediction models.

Materials and methods

An overview of the proposed pipeline is illustrated in Fig 1. Briefly, raw SAX and LAX images were first automatically segmented. Using the segmentations, contours and landmarks were extracted for each view. A biventricular surface mesh was then reconstructed using the contours and landmarks. The surface mesh was then converted to a volumetric mesh and the volumetric mesh was used to reconstruct cardiac fiber architecture and also mapped to universal ventricular coordinates.

Legal and ethical approval for the study is covered by the UK Biobank's Research Tissue Bank approval (REC reference 11/NW/0382 for the initial approval and renewals with REC references 16/NW/0274 and 21/NW/0157) obtained from the North West Multi-centre Research Ethics Committee (MREC). Our research project was approved by the UK Biobank in accordance with their application procedure.

Dataset

UK Biobank (UKBB) [28] is a large cohort study that includes CMR imaging and associated epidemiological and clinical data from >75,000 participants in the imaging substudy. The CMR imaging protocol has been described previously [29]. Briefly, steady-state free-precession CMR cine images were acquired in short and long axis locations, each with a separate breath-hold. Typical spatial resolution was 1.8x1.8x8mm for short axis and 1.6x1.6x6mm for long axis images. From this database, we utilized the following data for this study:

1. Long-axis (LAX) CMR images. These include images from three different views: 2-chamber, 3-chamber, and 4-chamber. Each view is a 2D + t (time) image with fifty time frames.
2. Short-axis (SAX) CMR images. Each SAX image is a 3D + t image with fifty time frames.

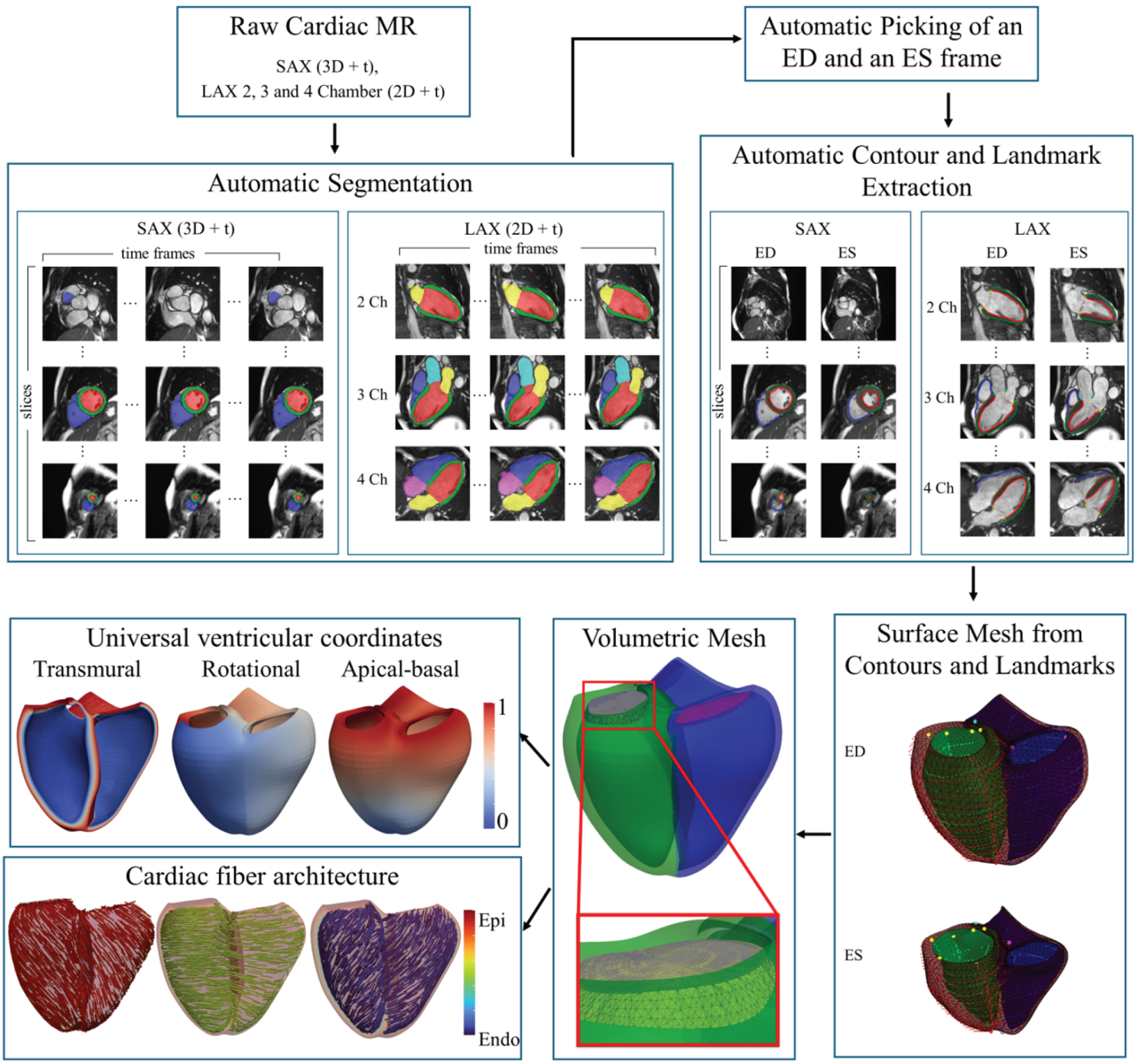

Fig 1. Overview. An overview of the proposed pipeline. Reproduced by kind permission of UK Biobank ©.

https://doi.org/10.1371/journal.pone.0327158.g001

3. Age, sex and body mass index (BMI) of participants.
4. Manual segmentations for the end-diastolic (ED) and end-systolic (ES) frames of the SAX view of 4788 participants. These manual segmentations were created in a previous study [29].
5. Various derived phenotypes such as ventricle volumes and ejection fractions reported in two previous studies for validation and comparison [29,30].

CMR images and SAX manual segmentations were downloaded from UKBB on March 2023 and other data were downloaded from UKBB on March 2024. For more details on the dataset, see S1 Table.

Preprocessing

The only preprocessing we performed was the conversion of raw DICOM files from UKBB corresponding to the LAX and SAX images, into NIFTI images. For each participant, four NIFTI files were created that corresponded to the four different CMR views: LAX 2-chamber, LAX 3-chamber, LAX 4-chamber, and SAX.

Segmentation

For each CMR view, a different set of heart structures were selected for segmentation as follows:

1. LAX 2-chamber: LV cavity, LV myocardium, LA cavity.
2. LAX 3-chamber: LV cavity, LV myocardium, RV cavity, RA cavity, Aorta
3. LAX 4-chamber: LV cavity, LV myocardium, RV cavity, LA cavity, RA cavity
4. SAX: LV cavity, LV myocardium, RV cavity

The structures to segment were selected based on how reliably they can be segmented from each view. RV myocardium, for example, is typically excluded from cine MR segmentation because it is too thin and usually gets lost to partial volume effect at typical cine MR resolution.

For the SAX view, we utilized manual segmentations that were previously created for the ED and ES frames in a previous study [29]. The identifier of 4788 participants could be matched between the manual segmentations and raw CMRs and these were used in this study. For the LAX views, we manually segmented 150 participants at the ED and ES frames selected in no particular order from the same set of 4788 participants. The segmentations were verified and corrected under the guidance of a CMR level 3 clinical practitioner. 4000 of the participants with manual SAX segmentations, and 100 of the participants with manual LAX segmentations were used for supervised training of segmentation networks. The remaining participants, 788 for SAX and 50 for LAX, were used as the test sets for evaluation. Training and test subjects were selected randomly.

For automatic segmentation, there are a wide variety of methods proposed in literature (see e.g. [31–35]). For this study, we picked the nnUNet [36] framework which implements self-configuring UNet-based [37] networks for medical image segmentation, and is reported to achieve state-of-the-art performance in various recent medical segmentation challenges [38–40]. The recommended usage of training five folds from the training set, and using all of them during inference was deployed separately for all views. Only 2D training was used for all views. Since LAX views are 2D, that is the only option, and for SAX, we chose to use only 2D because there was no clear evidence of 3D being better in a previous study that used nnUNet for CMR segmentation [41]. The ED and ES frames were treated as independent images for segmentation.

Automatic selection of ED and ES frames

The evaluation of segmentation accuracy, and subsequent meshing steps were performed for only the ED and ES frames because manual segmentations and previously reported reference derived phenotypes based on manual segmentations were only available for ED and ES frames, which makes validation and evaluation difficult for other frames. Hence, although the proposed pipeline could be applied to all time frames in principle, ED and ES frames were automatically selected after segmentation before subsequent steps. For the ED frame,

we simply selected the first time frame since that is the first frame acquired after the R wave detection in the UKBB CMR protocol, as done in [29]. For the ES frame, we picked the time frame for which the sum of voxel counts labelled as "LV cavity" in the LAX views, and the five mid-slices of the SAX view, was minimum. Automatic ES selection is illustrated for six example participants in Fig 2. The reason we did not use a similar algorithm for picking the ED frame as the frame with the maximum LV cavity volume is that, this algorithm is not perfect and can pick the wrong frame if the automatic segmentation fails in some of the time frames. For the UKBB dataset specifically, we think picking the first frame as the ED is more robust due to the UKBB imaging protocol. On other datasets where this is not the case however, picking the maximum LV cavity volume is a good alternative.

Extraction of contours and landmarks from the segmentation masks

After the ED and ES frames are selected, we then extracted the following contours and landmarks from each of the four CMR views using their segmentation masks:

1. LAX 2 chamber: Contours: LV endocardial, LV epicardial. Landmarks: Two points on the mitral valve plane, and the apex point, which is defined as the furthest point on the LV epicardial contour, from the mid-point between the two selected points on the mitral valve plane.
2. LAX 3 chamber: Contours: LV endocardial, LV epicardial, RV septum, RV free wall. Landmarks: Two points on the aorta-LV intersection, and two points on the mitral valve plane.

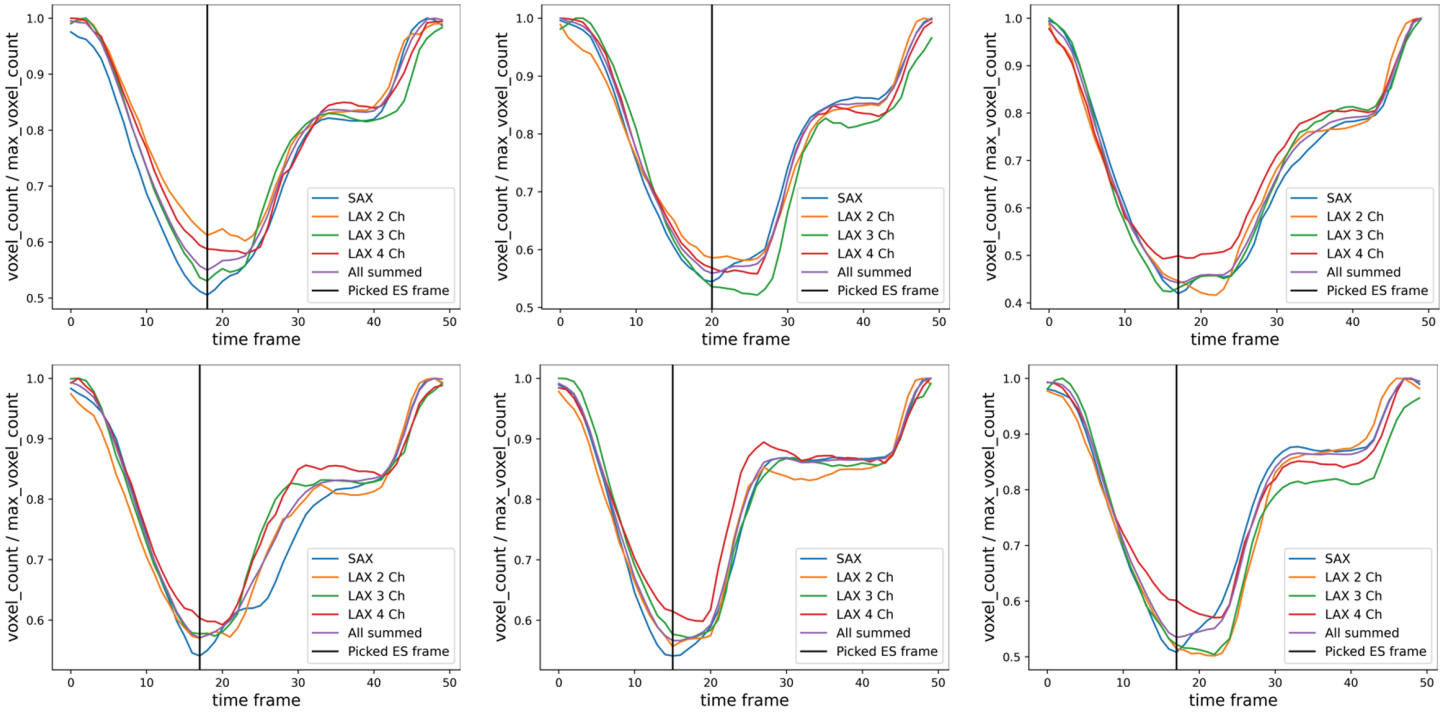

Fig 2. Picking the ES frame. The LV volume transients (LV voxel count on each time frame divided by the maximum LV voxel count across time frames) of six example participants for all the views separately, and their sum across the views. For the SAX view, only the five mid-slices were used for the calculation. The ES frame was picked as the time frame that minimizes the sum across all views.

https://doi.org/10.1371/journal.pone.0327158.g002

3. LAX 4 chamber: Contours: LV endocardial, LV epicardial, RV septum, RV free wall. Landmarks: Two points on the mitral valve plane, and two points on the tricuspid valve plane.
4. SAX: Contours: LV endocardial, LV epicardial, RV septum, RV free wall.

The contours and landmarks automatically extracted from the ED frame of a random participant are illustrated in Fig 3.

The extraction algorithm is based on simple heuristics, and the reader is referred to the source code and documentation for details.

Finite element mesh construction

We used an established Atlas-based pipeline [19] to construct the biventricular surface meshes. As the RV myocardium was not captured in the segmentation, during the surface mesh generation, the RV epicardium was estimated by extending the RV endocardium points

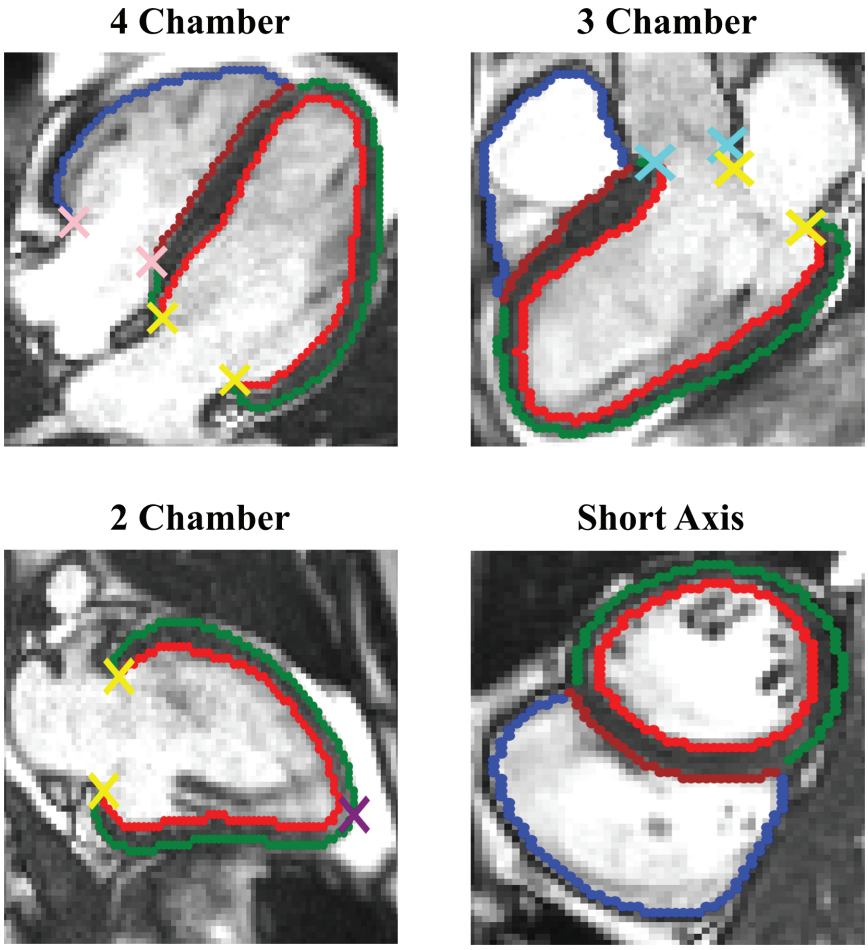

Fig 3. Contour and landmark extraction from segmentations. Illustration of contours and landmarks automatically extracted from the ED frame of a randomly selected participant. Contours: Red: LV endocardium, Green: LV epicardium, Brown: RV septum, Blue: RV free wall. Landmarks: Yellow: Points on the mitral valve, Pink: Points on the tricuspid valve, Teal: Points on the aorta-LV intersection, Purple: Apex. Reproduced by kind permission of UK Biobank ©.

https://doi.org/10.1371/journal.pone.0327158.g003

normal to the surfaces by 3 mm consistent with experimental measurements [42,43]. The resultant surface meshes were then used to construct tetrahedral finite element meshes using Meshtool [44] including six distinct regions of LV myocardium, RV myocardium, aortic, tricuspid, pulmonary and mitral valves.

All volumetric meshes were then incorporated with a morphological coordinate system, which describes the positions within ventricles based on the apical-basal (Z), transmural (ρ) (from endocardium to epicardium), rotational (Φ) (anterior, anteroseptal, inferior, inferolateral, anterolateral) and chamber-wise (left ventricle and right ventricle) coordinates [45]. For each mesh, it also includes a realistic biventricular myocardial fibre structure implemented using a rule-based approach with a transmural variation of angle α as from 60° to -60° in longitudinal fibre directions and angle β as from -65° to 25° in transverse fibre directions from endocardium to epicardium [46].

Representative mesh generation for different sex, age and BMI groups

Before constructing representative meshes, we employed a mesh quality control step to remove meshes that showed a large difference between surface-derived and segmentation-derived phenotypes from the SAX view. Specifically, LV and RV volumes, and LV myocardium mass were derived directly from nnUNet segmentations of the SAX view, and from surface meshes. The LV mass was computed from the end-diastolic LV myocardial volume using a density of 1.05 g/mL. The relative differences were then calculated between the phenotype derived directly from SAX segmentations and derived from surface meshes for each phenotype for the whole cohort. Finally, the participants for which the relative difference for at least one phenotype was greater than 75th percentile plus 1.5 times the interquartile range were not included in the construction of representative meshes.

Participants with viable surface meshes were categorized based on their demographics of sex, age and BMI. The age bins start with 44 with incremental of 1 year for each bin (i.e. 44, 45, 46…85) while the BMI bins start with 15 kg/m^2 with incremental of 1 kg/m^2 for each bin (i.e. 15,16,17,…,50). For each unique sex, age, BMI group with at least three participants, the 'average' surface mesh was constructed. Before averaging, all surface meshes were first registered to a common reference space to remove the inter-participant variability in orientations and positions using a Procrustes-based method. Specifically, we first randomly selected a participant's surface mesh as the reference and then superimposed all other surface meshes to this reference. To avoid the bias towards this reference, we computed the mean mesh of the set of superimposed meshes. Then the Procrustes distances between the mean mesh and the reference mesh were computed and if higher than 1e-6, the reference was updated as the mean mesh until the optimal reference mesh is found. In this way, we found the optimal reference mesh which represents the average heart position and orientation. Finally, all surface meshes were aligned with the optimal reference mesh and the average volumetric meshes for different bins were constructed along with their UVCs and ventricular fibres.

Results

Segmentation validation

The segmentation networks were validated in two ways: Comparison to manual segmentations using Dice scores, and comparison to previously reported derived phenotypes in literature such as volumes and ejection fraction. The participants in the test sets, 788 for SAX and 50 for LAX, were utilized for both of these comparisons.

Mean Dice scores for the test sets of each view for each segmented structure are given in Table 1. The automatic segmentations have high volumetric overlap with manual segmentations for every view and segmented structure.

Derived phenotypes

LV and RV volumes, and LV myocardium mass derived directly from manual, nnUNet-based and UNet-based (reported in [47]) SAX segmentations, and from surface meshes are compared to each other in Table 2. The number of participants used for this table was 731, which is smaller than the SAX test set size of 788 because it is also required that a UNet-based result exists for all the phenotypes and the surface reconstruction succeeds.

LA and RA volumes derived from from manual, nnUNet-based and UNet-based (reported in [47]) LAX segmentations are reported in Table 3. Since the meshes are biventricular, and hence do not include the atria, these cannot be derived from the meshes. The number of participants used for this table was 48, which is smaller than the LAX test set size of 50 because it is also required that a UNet-based result exists for all the phenotypes.

Application: Representative meshes

Surface meshes for the whole cohort were constructed from the end diastolic frames and used to build a cohort of representative meshes for specific gender, age and BMI bins. Fig 4(A) shows the number of females and males in the whole cohort, categorising into specific age (44 to 85 years old) and BMI (15 to 50 kg/m^2) bins. The bins that contained three or more participants were used to construct a representative mesh for that bin, resulting in a total number of 1423 representative meshes computed from 46917 individual meshes. Some example representative meshes are illustrated in Fig 5.

For details on the number of participants and meshes utilized at each step of the pipeline, see S2 Table.

We investigated the changes of cardiac structures with sex, BMI and age in the cohort of representative meshes. We computed three phenotypes: LVEDV, RVEDV and LV mass, and fitted a linear regression model for females and males with different age and BMI as shown in Fig 4(B) and 4(C). We found that all three phenotypes are greater for males than for females (LV mass: 133.6 $\pm$ 14.8 vs 97.2 $\pm$ 11.3 g; LVEDV: 154.5 $\pm$ 12.9 vs 121.0 $\pm$ 12.5 mL; RVEDV:

Table 1. Dice scores: Manual vs. nnUNet segmentations.

	2Ch	3Ch	4Ch	SAX
LV ED	0.97 (0.01)	0.98 (0.01)	0.97 (0.01)	0.97 (0.02)
LV ES	0.88 (0.10)	0.94 (0.06)	0.89 (0.09)	0.93 (0.04)
RV ED		0.95 (0.03)	0.95 (0.02)	0.93 (0.04)
RV ES		0.88 (0.08)	0.86 (0.10)	0.88 (0.05)
Myo ED	0.88 (0.02)	0.91 (0.03)	0.89 (0.03)	0.88 (0.03)
Myo ES	0.86 (0.09)	0.93 (0.07)	0.86 (0.09)	0.90 (0.03)
LA ED	0.90 (0.06)	0.96 (0.06)	0.89 (0.06)	
LA ES	0.95 (0.03)	0.98 (0.03)	0.95 (0.03)	
RA ED			0.92 (0.06)	
RA ES			0.96 (0.04)	
Ao ED		0.97 (0.02)		
Ao ES		0.96 (0.05)		

Mean and standard deviations of Dice scores between manual and nnUNet-produced segmentations. Empty cells mean that the structure is not segmented from the corresponding view.

https://doi.org/10.1371/journal.pone.0327158.t001

Table 2. Phenotypes derived from the SAX view.

(a) Value	Manual	nnUNet	UNet (Bai)	Mesh (Ours)
LVEDV (mL)	150.6 (34.2)	149.8 (33.4)	150.9 (33.3)	139.3 (30.8)
LVESV (mL)	63.1 (19.1)	62.3 (18.5)	62.4 (18.6)	59.6 (17.3)
LVM at ED (gram)	92.4 (24.4)	94.1 (23.2)	86.9 (21.8)	112.8 (25.4)
RVEDV (mL)	157.6 (38.7)	157.0 (37.6)	158.6 (38.0)	145.5 (34.9)
RVESV (mL)	70.4 (23.0)	68.9 (21.1)	69.4 (21.9)	64.0 (19.6)
LV EF (%)	58.4 (6.1)	58.7 (5.8)	59.0 (5.7)	57.6 (5.3)
RV EF (%)	55.9 (6.2)	56.5 (5.7)	56.7 (5.9)	56.5 (5.6)
(b) Absolute diff.	**nnUNet-Manual**	**UNet-Manual**	**nnUNet-UNet**	**nnUNet-Mesh**
LVEDV (mL)	6.0 (4.7)	5.9 (4.5)	2.5 (2.6)	11.1 (6.9)
LVESV (mL)	5.4 (4.8)	5.1 (4.6)	2.3 (2.9)	4.9 (3.9)
LVM at ED (gram)	7.1 (5.5)	8.2 (6.2)	7.2 (2.9)	18.8 (5.2)
RVEDV (mL)	7.9 (7.4)	8.2 (7.4)	4.4 (4.1)	12.0 (7.3)
RVESV (mL)	6.9 (6.8)	6.6 (6.4)	2.8 (2.6)	5.6 (4.1)
LV EF (%)	3.1 (2.8)	3.0 (2.8)	1.5 (2.0)	3.1 (2.7)
RV EF (%)	3.9 (3.3)	3.9 (3.1)	1.9 (1.8)	2.3 (2.2)
(c) Relative diff.	**nnUNet-Manual**	**UNet-Manual**	**nnUNet-UNet**	**nnUNet-Mesh**
LVEDV (%)	4.0 (3.0)	4.0 (2.9)	1.7 (1.8)	7.7 (4.7)
LVESV (%)	8.8 (7.5)	8.3 (7.3)	3.7 (4.6)	8.0 (5.7)
LVM at ED (%)	7.9 (6.3)	9.1 (6.5)	8.0 (2.7)	18.6 (4.8)
RVEDV (%)	5.0 (4.2)	5.1 (4.2)	2.7 (2.5)	8.0 (4.7)
RVESV (%)	9.9 (8.7)	9.6 (8.5)	4.1 (3.7)	8.6 (5.6)

Mean and standard deviations of the phenotypes derived from the SAX view with different methods, and their absolute and relative differences (n=731).

https://doi.org/10.1371/journal.pone.0327158.t002

Table 3. Phenotypes derived from the LAX views.

(a) Value	Manual (Petersen)	nnUNet	UNet(Bai)
LAMinV (mL)	29.0 (11.1)	31.0 (11.0)	30.5 (11.4)
LAMaxV (mL)	70.9 (21.3)	77.3 (22.1)	76.5 (21.8)
RAMinV (mL)	48.3 (20.8)	47.2 (17.2)	47.8 (18.8)
RAMaxV (mL)	79.7 (24.8)	84.9 (24.2)	86.9 (27.5)
(b) Absolute diff.	**nnUNet-Manual**	**UNet-Manual**	**nnUNet-UNet**
LAMinV (mL)	3.5 (2.7)	3.0 (2.4)	2.5 (2.2)
LAMaxV (mL)	8.1 (5.4)	6.6 (3.8)	4.4 (4.0)
RAMinV (mL)	4.7 (3.7)	3.9 (3.4)	2.9 (2.4)
RAMaxV (mL)	7.2 (5.0)	7.8 (6.3)	4.5 (4.6)
(c) Relative diff.	**nnUNet-Manual**	**UNet-Manual**	**nnUNet-UNet**
LAMinV (%)	12.5 (8.7)	10.9 (8.0)	9.0 (7.9)
LAMaxV (%)	11.3 (7.9)	9.2 (5.1)	5.8 (5.4)
RAMinV (%)	10.1 (6.9)	8.4 (6.7)	6.5 (6.0)
RAMaxV (%)	9.0 (6.5)	9.4 (5.8)	4.9 (3.8)

Mean and standard deviations of the phenotypes derived from the LAX views with different methods, and their absolute and relative differences (n=48).

https://doi.org/10.1371/journal.pone.0327158.t003

167.2 ± 13.5 vs 125.5 ± 12.8 mL, all $P < 0.0001$ from Mann-Whitney U test). Aging was associated with a reduction in both LV and RV diastolic volumes and LV mass (–0.8 and –0.7 mL/year and –0.3 g/year, β = 184, 188 and 130.5, $P = 5 \times 10^{-38}$, 4.6×10^{-23} and 4.6×10^{-5}). In contrast, increased BMI leads to an increase in LV and RV diastolic volumes and LV mass (1.1 and 1.2 mL/(kg/m^2) and 1.8 g/(kg/m^2), β =105.5, 110.1 and 64.5, $P=9.1 \times 10^{-39}$, 2.8×10^{-35} and 7.9×10^{-92}).

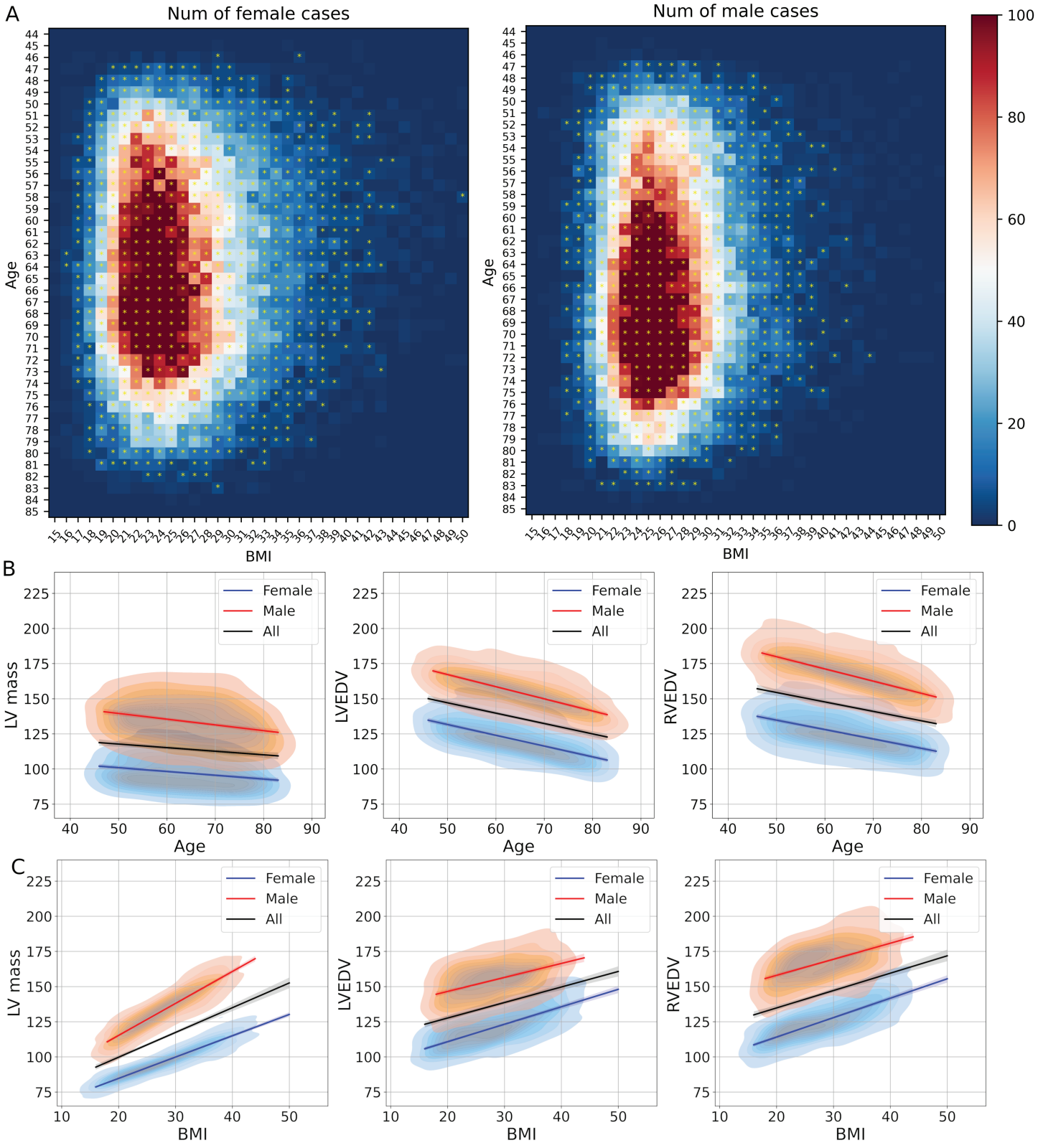

Fig 4. Demographic bins and associations with derived phenotypes. (A) The number of female and male participants in this cohort in specific age and BMI bins. The bins that contain more than three participants are marked with a * and a representative mesh is created for each of these bins. The colour bar represents the absolute value of the number of participants. (B),(C) Associations of derived phenotypes of all representative hearts with sex, age and BMI. The derived phenotypes LVEDV, RVEDV and LV mass are plotted as kernel density plots along with linear-regression lines for the whole cohort (black), for female (blue) and for male (red) (n=1423).

https://doi.org/10.1371/journal.pone.0327158.g004

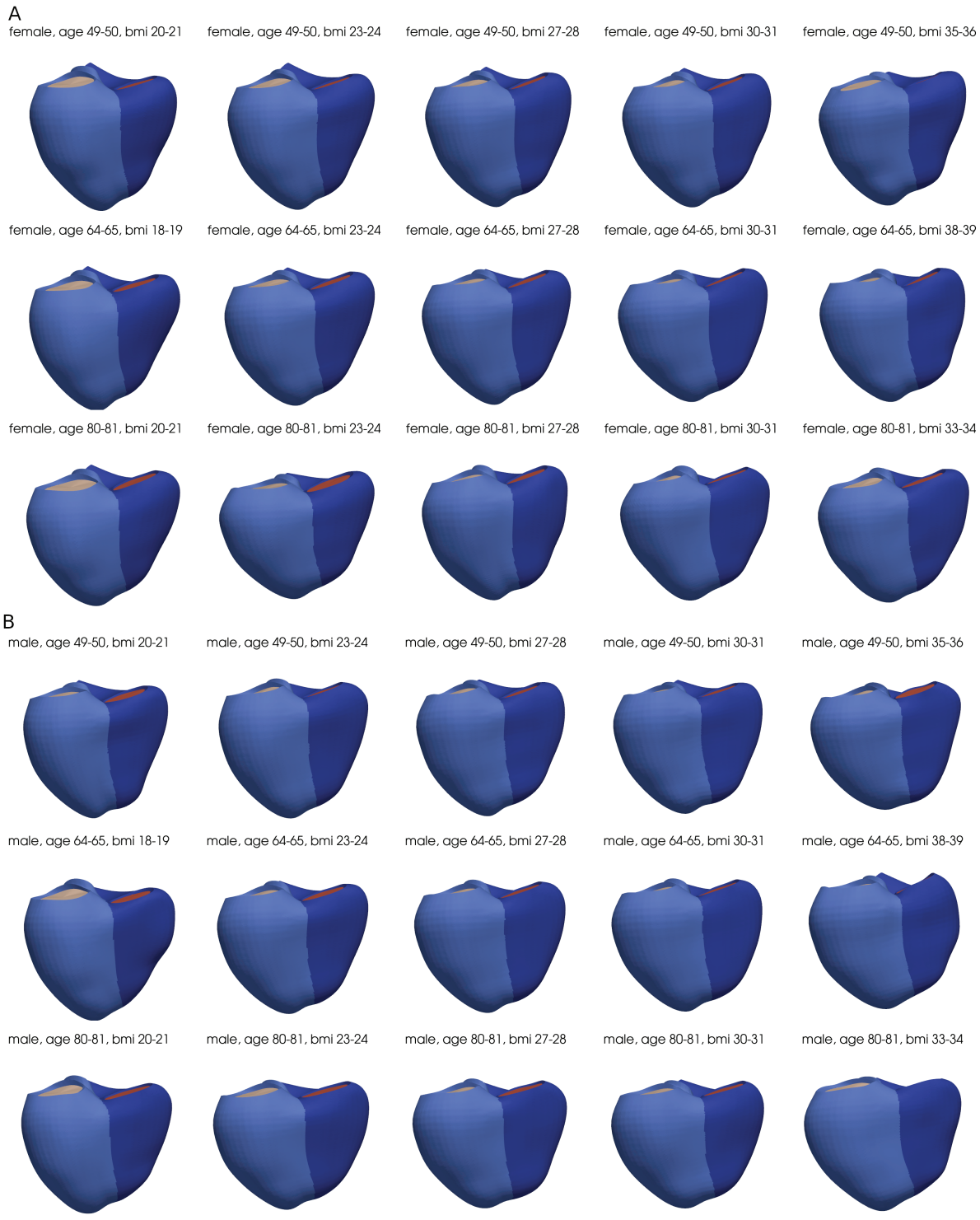

Fig 5. Examples of representative meshes for different demographic bins.

https://doi.org/10.1371/journal.pone.0327158.g005

Discussion

In this paper, we presented an automatic pipeline for CDT construction from raw cine MR images to biventricular meshes and validated it on the CMR data of 54926 participants from the UKBB. We also computed 1423 representative meshes and their corresponding fibers and UVCs from different sex, BMI, and age groupings from the UKBB. All the code used in the study, the trained segmentation networks, the representative meshes, and their corresponding fibers and UVCs are made publicly available. This will facilitate cardiac digital twinning from CMR images by providing an easily reproducible baseline for other researchers and readily usable meshes for mechanistic simulations and statistical prediction models.

Segmentation

The accuracy of the trained segmentation networks were validated using Dice scores and derived phenotypes. The Dice scores showed very good agreement between manual and automatic segmentations for all CMR views and structures. Due to the large time cost of manual segmentation, an inter-observer variability study was not conducted. In literature, [47] previously reported inter-observer variability on a set of SAX images of 50 subjects using three observers. Mean inter-observer Dice scores were 0.93 for LV, 0.88 for LV myocardium, and 0.88 for RV. The ED and ES scores were not reported separately, but it can be seen that our nnUNet-manual Dice scores are slightly higher if we average the ED and ES dice scores in Table 1 (0.95 for LV, 0.89 for LV myocardium, and 0.91 for RV).

It is worth noting that structures that are larger in the ED frame compared to the ES frame, such as the left and right ventricle cavities, tend to have a higher Dice score in the ED frame, and similarly, the atria which are smaller in the ED frame have a higher Dice score in the ES frame. This is not surprising since a volumetric overlap measure like Dice score tends to give higher scores for large connected structures due to the non-overlapping regions occurring only near the edges of the structure. For the LV myocardium, this effect is not clearly observed, which is likely due to the greater inherent ambiguity in the LV myocardium segmentation on the ES frame that causes a Dice score-reducing effect.

Derived phenotypes

The phenotypes derived from automatic vs. manual segmentations of the short-axis view showed similar agreement to the method presented in [47], which was reported to be comparable to inter-observer differences. This is not surprising since both methods are based on the U-Net architecture and trained using the manual segmentations from [29]. For the phenotypes derived from the long-axis, our method showed slightly higher difference to manual segmentations from [29] compared to the method from [47], but this is likely due to the fact that we trained our LAX networks using our own manual segmentations whereas [47]'s method was trained on [29]'s LAX segmentations.

As seen in Table 2, the phenotypes computed from the surface meshes showed a systematic bias in volumes and LV myocardial mass compared to segmentation-derived phenotypes from the nnUNet segmentations that were used to create the surface meshes. The mean of the LV-ED, LV-ES, RV-ED and RV-ES volumes computed from the meshes were respectively 7.0%, 4.3%, 7.3% and 7.1% smaller than the volumes computed from the nnUNet segmentations, and the mean of the LV myocardial mass was 19.9% larger. An underestimation of volumes and overestimation of the LV myocardial mass derived from meshes was previously reported in [48] with a smaller difference (4.1% smaller LV-ED volume and 6.6%

larger LV myocardial mass). One explanation of the difference is in the volume integration technique: the addition of disks from a short axis stack is different than the actual integration of volume from a 3D computational mesh. We would expect differences to be greater at the basal region of the anatomy. It is unclear at this stage how different meshing methods might affect this discrepancy and whether segmentation-derived or mesh-derived phenotypes should be preferred for a certain clinical application. Further study is required to address these questions. Interestingly, since the proportional volume underestimation is similar in the ED and ES frames, the difference in the LV and RV ejection fractions (important measures in clinical cardiology) remain comparable to the inter-observer variability reported in [47].

Representative meshes

The cohort of representative meshes was constructed by averaging the hearts of participants falling into same age, sex and BMI bins. The LV and RV end-diastolic volumes and LV mass derived from the representative meshes were found to decrease with aging and increase with larger BMI, which is consistent with previous studies measured from the general population of the UK Biobank [19,30] as well as other independent datasets [49]. Compared to the previously published virtual heart cohorts [6,24,50], this presented cohort (n=1423) is, to the best of our best knowledge, the largest heart cohort in the world which is additionally augmented with detailed demographics information such as sex, age and BMI, that can enable next generation population-specific studies. This cohort of anatomical-detailed representative models offers enriched heart shape information which provides a normative reference framework that can complement and strengthen the previous studies on biological age estimation [51–53], by enabling precise estimation of heart age deviation, supporting biological age acceleration analysis, improving prediction precision beyond radiomic approaches, and improving individualized cardiovascular risk profiling.

Limitations

Since the proposed method relies on segmentation networks trained with supervised learning, domain shift issues could negatively affect segmentation performance on different datasets. While the UKBB is a large dataset, all the participants are volunteers, and hence are likely to be healthier than patient cohorts from hospitals. Further, all UKBB CMR images are obtained using the same imaging protocol and scanner model. Therefore, when using a different dataset, domain shift is likely with respect to pathology composition of the cohort, imaging protocol, and scanner model. Possible domain shift issues are not addressed in this paper and will require further detailed studies.

As the RV wall thickness is difficult to estimate from only CMR images, we assumed a fixed 3 mm as the RV wall thickness, that can lead to inaccurate RV function estimation. We set the RV wall thickness as a variable in our pipeline which can be easily adjusted to allow flexible usage for any new studies if a personalized estimation of RV wall thickness is available.

The meshing method can produce intersections between the RV septum and the RV free wall surfaces, which causes failures in conversion from surface to volume meshes. Thus, some meshes may require post-processing before being used in simulations.

The proposed pipeline processes each time frame separately and temporal smoothness is not guaranteed or analysed. Hence, the method may not be readily suitable for functional twinning of the heart motion.

Conclusion

We presented an automatic pipeline from raw cine MR images to biventricular meshes and made publicly available all the code, trained segmentation networks and 1423 representative meshes and their corresponding fibers and UVCs from different sex, BMI, and age groupings from the UKBB. Future work is to create new representative cohorts for specific patient populations using the proposed pipeline, based on available individual data of summary diagnosis in the UKBB, enabling disease-specific studies. We anticipate this to be a valuable resource for other researchers working on cardiac digital twinning.

Supporting information

S1 Table. The dataset utilized from the UKBB.
(PDF)

S2 Table. Number of participants or meshes utilized at different steps of the pipeline. A number of participants or meshes were removed at certain steps of the pipeline due to reasons such as missing views, failing automatic quality-control checks, failing to produce an output etc. This table details the reasons for removal and the number of participants or meshes remaining after these removals.
(PDF)

S1 Fig. Bland-Altman plots for phenotypes derived from the SAX view.
(PDF)

Acknowledgments

This research has been conducted using the UK Biobank Resource under application number 88878.

Author contributions

Data curation: Bram Ruijsink.

Funding acquisition: Reza Razavi, Alistair Young, Pablo Lamata, Steven Niederer, Martin Bishop.

Methodology: Devran Ugurlu, Shuang Qian, Charlene Mauger, Laura Dal Toso, Yu Deng, Marina Strocchi.

Project administration: Reza Razavi, Alistair Young, Pablo Lamata, Steven Niederer, Martin Bishop.

Software: Devran Ugurlu, Shuang Qian, Elliot Fairweather, Charlene Mauger, Laura Dal Toso, Yu Deng, Marina Strocchi.

Supervision: Alistair Young, Pablo Lamata, Steven Niederer, Martin Bishop.

Validation: Devran Ugurlu, Shuang Qian, Elliot Fairweather, Bram Ruijsink.

Visualization: Devran Ugurlu, Shuang Qian, Elliot Fairweather.

Writing – original draft: Devran Ugurlu, Shuang Qian, Elliot Fairweather, Alistair Young, Pablo Lamata, Steven Niederer, Martin Bishop.

Writing – review & editing: Devran Ugurlu, Shuang Qian, Elliot Fairweather, Reza Razavi, Alistair Young, Pablo Lamata, Steven Niederer, Martin Bishop.

References

1. Joseph P, Leong D, McKee M, Anand SS, Schwalm J-D, Teo K, et al. Reducing the global burden of cardiovascular disease, Part 1: The epidemiology and risk factors. Circ Res. 2017;121(6):677–94. https://doi.org/10.1161/CIRCRESAHA.117.308903 PMID: 28860318
2. Corral-Acero J, Margara F, Marciniak M, Rodero C, Loncaric F, Feng Y, et al. The "Digital Twin" to enable the vision of precision cardiology. Eur Heart J. 2020;41(48):4556–64. https://doi.org/10.1093/eurheartj/ehaa159 PMID: 32128588
3. Coorey G, Figtree GA, Fletcher DF, Snelson VJ, Vernon ST, Winlaw D, et al. The health digital twin to tackle cardiovascular disease-a review of an emerging interdisciplinary field. NPJ Digit Med. 2022;5(1):126. https://doi.org/10.1038/s41746-022-00640-7 PMID: 36028526
4. Viola F, Del Corso G, De Paulis R, Verzicco R. GPU accelerated digital twins of the human heart open new routes for cardiovascular research. Sci Rep. 2023;13(1):8230. https://doi.org/10.1038/s41598-023-34098-8 PMID: 37217483
5. Zaidi H, Jones R, Campos FO, Qian S, Young A, Plank G, et al. MP-470543-006 towards a global arrhythmic risk score for icd placement in ischemic heart disease incorporating novel computational-derived biomarkers. Heart Rhythm. 2024;21(5):S54–5. https://doi.org/10.1016/j.hrthm.2024.03.369
6. Qian S, Monaci S, Mendonca-Costa C, Campos F, Gemmell P, Zaidi HA, et al. Additional coils mitigate elevated defibrillation threshold in right-sided implantable cardioverter defibrillator generator placement: a simulation study. Europace. 2023;25(6):euad146. https://doi.org/10.1093/europace/euad146 PMID: 37314196
7. Monaci S, Qian S, Gillette K, Puyol-Antón E, Mukherjee R, Elliott MK, et al. Non-invasive localization of post-infarct ventricular tachycardia exit sites to guide ablation planning: a computational deep learning platform utilizing the 12-lead electrocardiogram and intracardiac electrograms from implanted devices. Europace. 2023;25(2):469–77. https://doi.org/10.1093/europace/euac178 PMID: 36369980
8. Mauger CA, Gilbert K, Suinesiaputra A, Bluemke DA, Wu CO, Lima JAC, et al. Multi-ethnic study of atherosclerosis: relationship between left ventricular shape at cardiac MRI and 10-year outcomes. Radiology. 2023;306(2):e220122. https://doi.org/10.1148/radiol.220122 PMID: 36125376
9. Qian S, Ugurlu D, Fairweather E, Toso LD, Deng Y, Strocchi M, et al. Developing cardiac digital twin populations powered by machine learning provides electrophysiological insights in conduction and repolarization. Nat Cardiovasc Res. 2025;4(5):624–36. https://doi.org/10.1038/s44161-025-00650-0 PMID: 40379795
10. Ruijsink B, Puyol-Antón E, Oksuz I, Sinclair M, Bai W, Schnabel JA, et al. Fully automated, quality-controlled cardiac analysis from CMR: validation and large-scale application to characterize cardiac function. JACC Cardiovasc Imaging. 2020;13(3):684–95. https://doi.org/10.1016/j.jcmg.2019.05.030 PMID: 31326477
11. von Knobelsdorff-Brenkenhoff F, Pilz G, Schulz-Menger J. Representation of cardiovascular magnetic resonance in the AHA/ACC guidelines. J Cardiovasc Magn Reson. 2017;19(1):70. https://doi.org/10.1186/s12968-017-0385-z PMID: 28942735
12. Villard B, Grau V, Zacur E. Surface mesh reconstruction from cardiac MRI contours. J Imaging. 2018;4(1):16. https://doi.org/10.3390/jimaging4010016
13. Banerjee A, Camps J, Zacur E, Andrews CM, Rudy Y, Choudhury RP, et al. A completely automated pipeline for 3D reconstruction of human heart from 2D cine magnetic resonance slices. Philos Trans A Math Phys Eng Sci. 2021;379(2212):20200257. https://doi.org/10.1098/rsta.2020.0257 PMID: 34689630
14. Küstner T, Fuin N, Hammernik K, Bustin A, Qi H, Hajhosseiny R, et al. CINENet: deep learning-based 3D cardiac CINE MRI reconstruction with multi-coil complex-valued 4D spatio-temporal convolutions. Sci Rep. 2020;10(1):13710. https://doi.org/10.1038/s41598-020-70551-8 PMID: 32792507
15. Sandino CM, Lai P, Vasanawala SS, Cheng JY. Accelerating cardiac cine MRI using a deep learning-based ESPIRiT reconstruction. Magn Reson Med. 2021;85(1):152–67. https://doi.org/10.1002/mrm.28420 PMID: 32697891
16. Hammernik K, Küstner T, Yaman B, Huang Z, Rueckert D, Knoll F, et al. Physics-driven deep learning for computational magnetic resonance imaging: combining physics and machine learning for improved medical imaging. IEEE Signal Process Mag. 2023;40(1):98–114. https://doi.org/10.1109/msp.2022.3215288 PMID: 37304755
17. Lamata P, Niederer S, Nordsletten D, Barber DC, Roy I, Hose DR, et al. An accurate, fast and robust method to generate patient-specific cubic Hermite meshes. Med Image Anal. 2011;15(6):801–13. https://doi.org/10.1016/j.media.2011.06.010 PMID: 21788150

18. Mauger C, Gilbert K, Suinesiaputra A, Pontre B, Omens J, McCulloch A, et al. An iterative diffeomorphic algorithm for registration of subdivision surfaces: application to congenital heart disease. Annu Int Conf IEEE Eng Med Biol Soc. 2018;2018:596–9. https://doi.org/10.1109/EMBC.2018.8512394 PMID: 30440467

19. Mauger C, Gilbert K, Lee AM, Sanghvi MM, Aung N, Fung K, et al. Right ventricular shape and function: cardiovascular magnetic resonance reference morphology and biventricular risk factor morphometrics in UK Biobank. J Cardiovasc Magn Reson. 2019;21(1):41. https://doi.org/10.1186/s12968-019-0551-6 PMID: 31315625

20. Beetz M, Banerjee A, Grau V. Biventricular surface reconstruction from cine MRI contours using point completion networks. In: 2021 IEEE 18th International Symposium on Biomedical Imaging (ISBI). 2021. p. 105–9. https://doi.org/10.1109/isbi48211.2021.9434040

21. Banerjee A, Zacur E, Choudhury RP, Grau V. Automated 3D whole-heart mesh reconstruction from 2D cine MR slices using statistical shape model. Annu Int Conf IEEE Eng Med Biol Soc. 2022;2022:1702–6. https://doi.org/10.1109/EMBC48229.2022.9871327 PMID: 36086304

22. Hoogendoorn C, Duchateau N, Sánchez-Quintana D, Whitmarsh T, Sukno FM, De Craene M, et al. A high-resolution atlas and statistical model of the human heart from multislice CT. IEEE Trans Med Imaging. 2013;32(1):28–44. https://doi.org/10.1109/TMI.2012.2230015 PMID: 23204277

23. Xia Y, Chen X, Ravikumar N, Kelly C, Attar R, Aung N, et al. Automatic 3D+t four-chamber CMR quantification of the UK biobank: integrating imaging and non-imaging data priors at scale. Med Image Anal. 2022;80:102498. https://doi.org/10.1016/j.media.2022.102498 PMID: 35665663

24. Rodero C, Strocchi M, Marciniak M, Longobardi S, Whitaker J, O'Neill MD, et al. Linking statistical shape models and simulated function in the healthy adult human heart. PLoS Comput Biol. 2021;17(4):e1008851. https://doi.org/10.1371/journal.pcbi.1008851 PMID: 33857152

25. Gaggion N, Matheson BA, Xia Y, Bonazzola R, Ravikumar N, Taylor ZA. Multi-view hybrid graph convolutional network for volume-to-mesh reconstruction in cardiovascular MRI. 2023.

26. Kong F, Wilson N, Shadden S. A deep-learning approach for direct whole-heart mesh reconstruction. Med Image Anal. 2021;74:102222. https://doi.org/10.1016/j.media.2021.102222 PMID: 34543913

27. Kong F, Shadden SC. Learning whole heart mesh generation from patient images for computational simulations. IEEE Trans Med Imaging. 2023;42(2):533–45. https://doi.org/10.1109/TMI.2022.3219284 PMID: 36327186

28. Sudlow C, Gallacher J, Allen N, Beral V, Burton P, Danesh J, et al. UK biobank: an open access resource for identifying the causes of a wide range of complex diseases of middle and old age. PLoS Med. 2015;12(3):e1001779. https://doi.org/10.1371/journal.pmed.1001779 PMID: 25826379

29. Petersen SE, Aung N, Sanghvi MM, Zemrak F, Fung K, Paiva JM, et al. Reference ranges for cardiac structure and function using cardiovascular magnetic resonance (CMR) in Caucasians from the UK Biobank population cohort. J Cardiovasc Magn Reson. 2017;19(1):18. https://doi.org/10.1186/s12968-017-0327-9 PMID: 28178995

30. Bai W, Suzuki H, Huang J, Francis C, Wang S, Tarroni G, et al. A population-based phenome-wide association study of cardiac and aortic structure and function. Nat Med. 2020;26(10):1654–62. https://doi.org/10.1038/s41591-020-1009-y PMID: 32839619

31. Chen C, Qin C, Qiu H, Tarroni G, Duan J, Bai W, et al. Deep learning for cardiac image segmentation: a review. Front Cardiovasc Med. 2020;7:25. https://doi.org/10.3389/fcvm.2020.00025 PMID: 32195270

32. Ammar A, Bouattane O, Youssfi M. Automatic cardiac cine MRI segmentation and heart disease classification. Comput Med Imaging Graph. 2021;88:101864. https://doi.org/10.1016/j.compmedimag.2021.101864 PMID: 33485057

33. Tayebi Arasteh S, Romanowicz J, Pace DF, Golland P, Powell AJ, Maier AK, et al. Automated segmentation of 3D cine cardiovascular magnetic resonance imaging. Front Cardiovasc Med. 2023;10:1167500. https://doi.org/10.3389/fcvm.2023.1167500 PMID: 37904806

34. El-Taraboulsi J, Cabrera CP, Roney C, Aung N. Deep neural network architectures for cardiac image segmentation. Artif Intell Life Sci. 2023;4:100083. https://doi.org/10.1016/j.ailsci.2023.100083

35. Alnasser TN, Abdulaal L, Maiter A, Sharkey M, Dwivedi K, Salehi M, et al. Advancements in cardiac structures segmentation: a comprehensive systematic review of deep learning in CT imaging. Front Cardiovasc Med. 2024;11:1323461. https://doi.org/10.3389/fcvm.2024.1323461 PMID: 38317865

36. Isensee F, Jaeger PF, Kohl SAA, Petersen J, Maier-Hein KH. nnU-Net: a self-configuring method for deep learning-based biomedical image segmentation. Nat Methods. 2021;18(2):203–11. https://doi.org/10.1038/s41592-020-01008-z PMID: 33288961

37. Ronneberger O, Fischer P, Brox T. U-Net: convolutional networks for biomedical image segmentation. In: Medical Image Computing and Computer-Assisted Intervention – MICCAI 2015. Cham: Springer; 2015. p. 234–41.

38. Campello VM, Gkontra P, Izquierdo C, Martin-Isla C, Sojoudi A, Full PM, et al. Multi-centre, multi-vendor and multi-disease cardiac segmentation: the M&Ms challenge. IEEE Trans Med Imaging. 2021;40(12):3543–54. https://doi.org/10.1109/TMI.2021.3090082 PMID: 34138702

39. Ji Y, Bai H, Yang J, Ge C, Zhu Y, Zhang R, et al. AMOS: a large-scale abdominal multi-organ benchmark for versatile medical image segmentation; 2022.

40. Martin-Isla C, Campello VM, Izquierdo C, Kushibar K, Sendra-Balcells C, Gkontra P, et al. Deep learning segmentation of the right ventricle in cardiac MRI: the M&Ms challenge. IEEE J Biomed Health Inform. 2023;27(7):3302–13. https://doi.org/10.1109/JBHI.2023.3267857 PMID: 37067963

41. Full P, Isensee F, Jäger PF, Maier-Hein K. Studying robustness of semantic segmentation under domain shift in cardiac MRI. In: Puyol Anton E, Pop M, Sermesant M, Campello V, Lalande A, Lekadir K, editors. Statistical atlases and computational models of the heart. M&Ms and EMIDEC challenges. Cham: Springer; 2021. p. 238–49.

42. Matsukubo H, Matsuura T, Endo N, Asayama J, Watanabe T. Echocardiographic measurement of right ventricular wall thickness. A new application of subxiphoid echocardiography. Circulation. 1977;56(2):278–84. https://doi.org/10.1161/01.cir.56.2.278 PMID: 872322

43. Ho S, Nihoyannopoulos P. Anatomy, echocardiography, and normal right ventricular dimensions. Heart. 2006;92(suppl 1):i2–13.

44. Neic A, Gsell MAF, Karabelas E, Prassl AJ, Plank G. Automating image-based mesh generation and manipulation tasks in cardiac modeling workflows using Meshtool. SoftwareX. 2020;11:100454. https://doi.org/10.1016/j.softx.2020.100454 PMID: 32607406

45. Bayer J, Prassl AJ, Pashaei A, Gomez JF, Frontera A, Neic A, et al. Universal ventricular coordinates: a generic framework for describing position within the heart and transferring data. Med Image Anal. 2018;45:83–93. https://doi.org/10.1016/j.media.2018.01.005 PMID: 29414438

46. Bayer JD, Blake RC, Plank G, Trayanova NA. A novel rule-based algorithm for assigning myocardial fiber orientation to computational heart models. Ann Biomed Eng. 2012;40(10):2243–54. https://doi.org/10.1007/s10439-012-0593-5 PMID: 22648575

47. Bai W, Sinclair M, Tarroni G, Oktay O, Rajchl M, Vaillant G, et al. Automated cardiovascular magnetic resonance image analysis with fully convolutional networks. J Cardiovasc Magn Reson. 2018;20(1):65. https://doi.org/10.1186/s12968-018-0471-x PMID: 30217194

48. Marciniak M, van Deutekom AW, Toemen L, Lewandowski AJ, Gaillard R, Young AA, et al. A three-dimensional atlas of child's cardiac anatomy and the unique morphological alterations associated with obesity. Eur Heart J Cardiovasc Imaging. 2022;23(12):1645–53. https://doi.org/10.1093/ehjci/jeab271 PMID: 34931224

49. Wade KH, Chiesa ST, Hughes AD, Chaturvedi N, Charakida M, Rapala A, et al. Assessing the causal role of body mass index on cardiovascular health in young adults: Mendelian randomization and recall-by-genotype analyses. Circulation. 2018;138(20):2187–201. https://doi.org/10.1161/CIRCULATIONAHA.117.033278 PMID: 30524135

50. Strocchi M, Augustin CM, Gsell MAF, Karabelas E, Neic A, Gillette K, et al. A publicly available virtual cohort of four-chamber heart meshes for cardiac electro-mechanics simulations. PLoS One. 2020;15(6):e0235145. https://doi.org/10.1371/journal.pone.0235145 PMID: 32589679

51. Mao R, Wang F, Zhong Y, Meng X, Zhang T, Li J. Association of biological age acceleration with cardiac morphology, function, and incident heart failure: insights from UK Biobank participants. Eur Heart J Cardiovasc Imaging. 2024;25(9):1315–23. https://doi.org/10.1093/ehjci/jeae126 PMID: 38747402

52. Raisi-Estabragh Z, Salih A, Gkontra P, Atehortúa A, Radeva P, Boscolo Galazzo I, et al. Estimation of biological heart age using cardiovascular magnetic resonance radiomics. Sci Rep. 2022;12(1):12805. https://doi.org/10.1038/s41598-022-16639-9 PMID: 35896705

53. Ecker V, Früh M, Yang B, Gatidis S, Küstner T. Deep regression for biological age estimation in multiple organs: investigations on 40,000 subjects of the UK Biobank. In: ICASSP 2024 - 2024 IEEE International Conference on Acoustics, Speech and Signal Processing (ICASSP); 2024. p. 2255–9.